ACS central science

Research Article

Cite This: ACS Cent. Sci. 2018, 4, 216−222

Chemical Stabilization of Perovskite Solar Cells with Functional Fulleropyrrolidines

Yao Liu,[†,‡] Zachariah A. Page,[†,§] Dongming Zhou,[∥] Volodimyr V. Duzhko,[†] Kevin R. Kittilstved,[∥] Todd Emrick,*[,†] and Thomas P. Russell*[,†,‡]

[†]Polymer Science and Engineering Department, University of Massachusetts Amherst, 120 Governors Drive, Amherst, Massachusetts 01003, United States

[‡]Beijing Advanced Innovation Center for Soft Matter Science and Engineering, Beijing University of Chemical Technology, Beijing, 100029, China

[∥]Department of Chemistry, University of Massachusetts Amherst, 710 North Pleasant Street, Amherst, Massachusetts 01003, United States

Supporting Information

ABSTRACT: While perovskite solar cells have invigorated the photovoltaic research community due to their excellent power conversion efficiencies (PCEs), these devices notably suffer from poor stability. To address this crucial issue, a solution-processable organic chemical inhibition layer (OCIL) was integrated into perovskite solar cells, resulting in improved device stability and a maximum PCE of 16.3%. Photoenhanced self-doping of the fulleropyrrolidine mixture in the interlayers afforded devices that were advantageously insensitive to OCIL thickness, ranging from 4 to 190 nm. X-ray photoelectron spectroscopy (XPS) indicated that the fulleropyrrolidine mixture improved device stability by stabilizing the metal electrode and trapping ionic defects (i.e., I^-) that originate from the perovskite active layer. Moreover, degraded devices were rejuvenated by repeatedly peeling away and replacing the OCIL/Ag electrode, and this repeel and replace process resulted in further improvement to device stability with minimal variation of device efficiency.

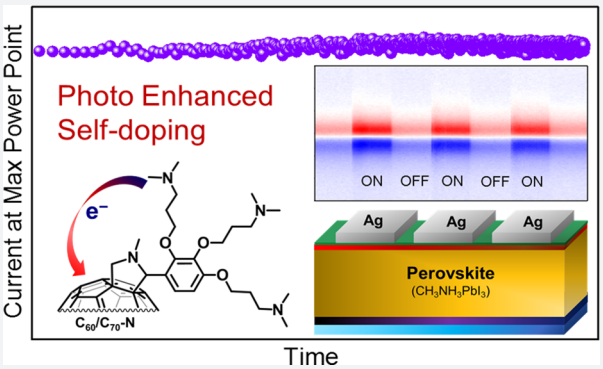

INTRODUCTION

Organometallic trihalide perovskites (OTPs) afford efficient active layer materials in photovoltaic devices,[1−5] yielding certified power conversion efficiency (PCE) values exceeding 20%.[6−16] Although the efficiency of perovskite-based devices has improved rapidly,[17] key fundamental issues remain, most notably pertaining to device stability.[18,19] Snaith and co-workers reported that degradation of OTPs by external contaminants (e.g., water) can be mitigated by device encapsulation in an inert atmosphere, as suggested by little-to-no change in visible light absorption over extended exposure (∼1000 h) to simulated sunlight.[20] However, integrating perovskites into multilayered photovoltaic devices opens new pathways for potential degradation arising from charge selective transport layers, ionic defects in the perovskite layer, and metal electrodes.[21−24]

Titanium dioxide (TiO_2) is a commonly used electron transport layer (ETL) for perovskite-based photovoltaic devices. However, UV excitation induces a high density of trap states and causes significant device deterioration.[25] Similarly, doped hole transport layers (HTLs) improve perovskite device performance, but ultimately device lifetime suffers as the perovskite reacts with dopants and decomposes.[21] Recently, device stability has been improved by inserting nondoped charge transport layers, such as fullerene derivatives,[26−28] zinc oxide nanocrystals,[29] and conjugated small molecules and polymers,[30−36] between the perovskite and electrode. Although interlayers and encapsulation methods improve device stability, the greatest challenges remain from ion contamination inherent to the polycrystalline perovskite films (e.g., halide or methylammonium ions).[37,38] For example, Guerrero et al. found that ionic defects lead to "self-degradation" over time by ion migration from the perovskite active layers to the electrode/ETL interface, causing charge buildup that impedes electron extraction and diminishes device performance.[39] An elegant method to overcome this issue was developed by Back et al., in which an amine-containing titanium suboxide (Am-TiO_x) sol−gel chemical inhibition layer (CIL) served to extract and stabilize the ionic defects.[37]

We have been investigating functional fullerenes and fulleropyrrolidines as solution-processable organic chemical

Received: September 28, 2017
Published: December 27, 2017

DOI: 10.1021/acscentsci.7b00454
ACS Cent. Sci. 2018, 4, 216−222

inhibition layers (OCIL) in perovskite solar cells. These fulleropyrrolidines demonstrate unique photoenhanced self-doping properties that efficiently modulate material conductivity and afford high performance perovskite solar cells across a wide range of OCIL thickness. In addition to providing superior processing advantages, such as precluding the need for thermal annealing and passivating sublayers and metal electrodes, this work enables the removal of ionic defects extracted into the OCIL by peeling away the OCIL/cathode, then replacing it, with little-to-no decrease in device performance. Consequently, degraded devices can be rejuvenated by repeatedly peeling away and replacing the OCIL/Ag electrode, resulting in significant recovery of device efficiency and improved stability over numerous cycles.

RESULTS AND DISCUSSION

Fulleropyrrolidines were selected as OCILs for their advantageous features, including (1) excellent electron transport and

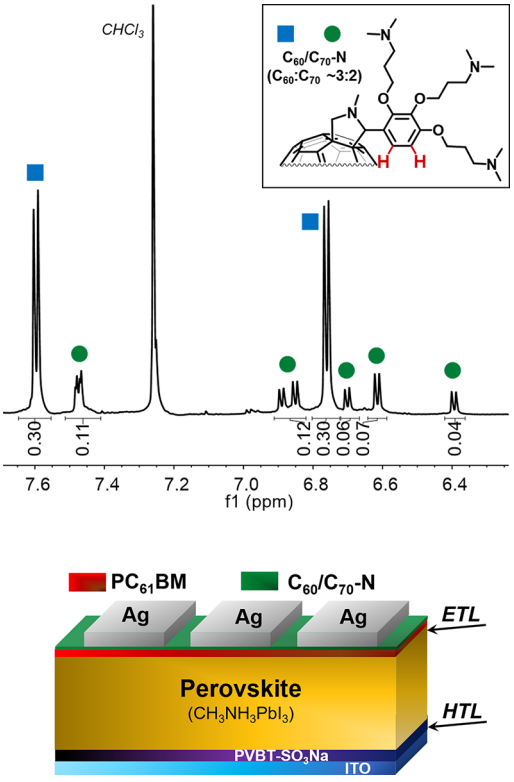

Figure 1. Top: ^{1}H NMR spectrum of C_{60}/C_{70}-N in $CDCl_3$, showing aromatic protons from C_{60}-N (blue squares) and C_{70}-N (green circles). Bottom: Device structure and composition for the perovskite-based photovoltaics studied.

film forming properties; (2) efficient electron extraction at the OCIL/metal interface due to a large interfacial dipole (Δ);[40] and (3) the presence of amine functionality for trapping transient ionic contaminants (e.g., I^-) from the perovskite active layer.[37] We selected a C_{60}/C_{70} mixture instead of pure C_{60}, since the mixture exhibits excellent performace and is more economical ($C_{60} \approx$ \$50/g vs $C_{60}/C_{70} <$ \$15/g).[41] Amine-substituted C_{60}/C_{70} fulleropyrrolidines were synthesized by Mitsunobu coupling of 2,3,4-trihydroxybenzaldehyde and 3-dimethylaminopropan-1-ol to yield 2,3,4-tris(3-(dimethylamino)propoxy)benzaldehyde, which was employed in a Prato reaction using the fullerene mixture and sarcosine (see synthesis in Supporting Information). Matrix-assisted laser desorption/ionization time-of-flight (MALDI-TOF) mass spectrometry confirmed the presence of both the C_{60}-N and C_{70}-N adducts, while ^{1}H NMR and UV/vis absorption spectroscopies characterized the ratio of the two components (C_{60}:$C_{70} \approx$ 3:2, see Figure 1 and Figures S1–S3). The aromatic protons identified in the ^{1}H NMR spectrum distinguish C_{60}-N and C_{70}-N by the chirality and asymmetry of the fulleropyrrolidine–C_{70} adducts that produce multiple resonances with complex coupling patterns.[42] Different reactivity across the two [6–6] ring-fusion bonds (a.k.a., [6–6] α- and β-type) results from the asymmetry of C_{70} and affords two sets of [6–6] monoadducts.[43]

Fullerene/perovskite planar heterojunction solar cells, shown in Figure 1, were fabricated by depositing an anionic poly(phenylenevinylene) (PVBT-SO_3Na, Figure S4) onto indium tin oxide (ITO) as an efficient water-soluble HTL for perovskite solar cells.[44,45] The perovskite layer was prepared by spin-coating a solution of $Pb(OAc)_2$ and methylammonium iodide (MAI) (1:3 molar ratio, 650 mg/mL in total) in *N*,*N*-dimethylformamide (DMF) onto the HTL/ITO substrates at a spin speed of 2000 rpm for 60 s inside a glovebox (N_2 atmosphere, <1 ppm of O_2, <1 ppm of H_2O), followed by mild thermal annealing (90 °C, 5 min) to form the polycrystalline perovskite layer (film thickness ≈300 nm). The perovskite film is quite uniform and smooth as shown in Figure S5. Subsequently, phenyl-C_{61}-butyric acid methyl ester ($PC_{61}BM$) was applied by spin-coating onto the perovskite layer from chlorobenzene, which acts as the ETL (film thickness: ∼60 nm), followed by spin-coating of the C_{60}-N or mixed C_{60}/C_{70}-N OCIL from 2,2,2-trifluoroethanol (TFE) at a variety of film thicknesses (a representative cross-sectional image of the device is provided in Figure S4). The Ag cathodes were then applied by thermal evaporation onto the fulleropyrrolidine interlayer to complete the device.

As shown in Figure 2A, devices containing mixed C_{60}/C_{70}-N (∼60 nm) gave a maximum PCE of 16.3% with an open circuit voltage (V_{OC}) of 0.95 V, a short circuit current density (J_{SC}) of 22.6 mA cm^{-2}, and a fill factor (FF) of 76%. No visible J–V hysteresis was observed under forward and reverse voltage scans, which was comparable to devices made with pure C_{60}-N as shown in Figure S6A. For comparison, devices containing C_{60}/C_{70}-N as the ETL directly coated onto the perovskite layer only gave an optimal PCE of 13.2% (Figure S6B). The control device, without the interlayer, produced a far lower peak PCE of 9.2%, with a pronounced S-shape to the J–V curve, and significant hysteresis (Figure 2A). The high external quantum efficiency (EQE) values in Figure 2B demonstrate a broad photoresponse, extending to ∼800 nm, with values exceeding 90% from ∼500 to 740 nm. The dependence of device performance on interlayer thickness was investigated by spin-coating C_{60}/C_{70}-N solutions of varying concentrations (1–40 mg/mL) onto the same perovskite/$PC_{61}BM$ layer, resulting in C_{60}/C_{70}-N OCIL thicknesses ranging from ∼4 to ∼190 nm. As shown in Figure 2C, V_{OC} and FF remained relatively constant with increasing OCIL thickness. An interlayer thickness of ∼60 nm afforded the maximum J_{SC} value and optimal PCE (16.3%), while further increasing the layer thickness caused a decrease in J_{SC} and overall device performance. Notably, devices maintained PCE values in excess of 12% across all OCIL thicknesses tested, with device metrics summarized in Table 1. Overall, this excellent tolerance to interlayer thickness represents an important feature for widening the processing window of

DOI: 10.1021/acscentsci.7b00454
ACS Cent. Sci. 2018, 4, 216–222

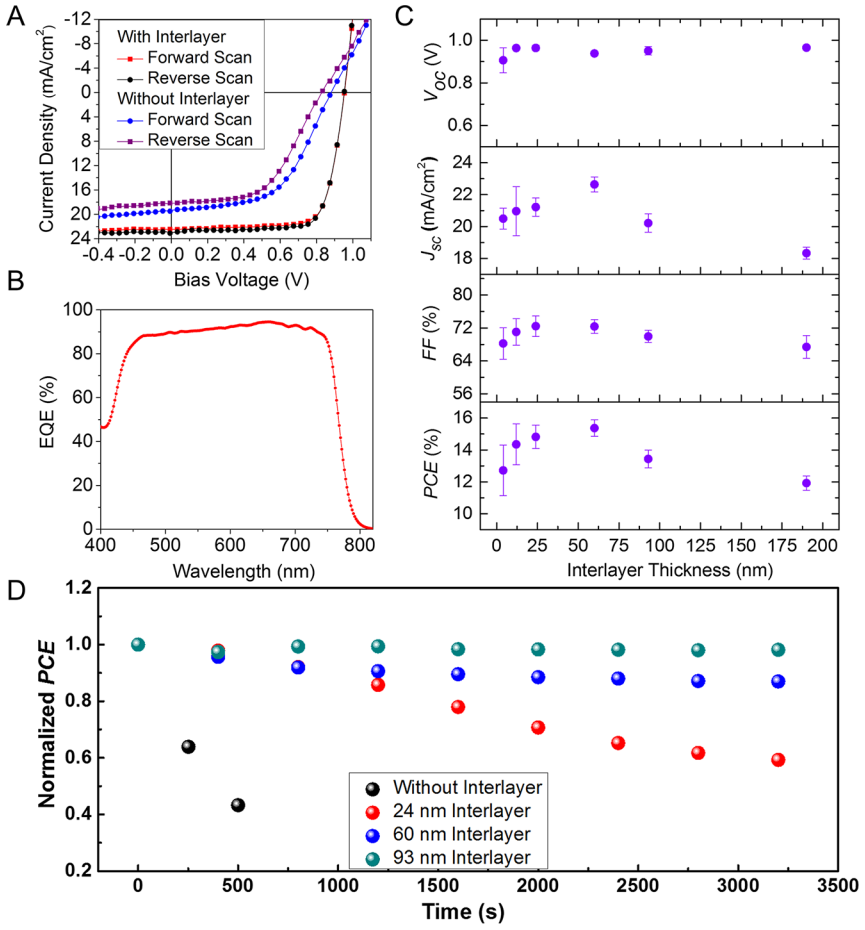

Figure 2. Photovoltaic performance. (A) J–V curves of the optimized perovskite devices with and without a C_{60}/C_{70}-N interlayer; (B) the corresponding EQE profile of the optimal device; (C) device performance as a function of interlayer thickness (error represents ±1 standard deviation from 8 devices; devices for OCIL thickness measurements were prepared at the same time using the same batch of perovskite precursors); (D) normalized PCE of devices with different interlayer thicknesses as a function of time under MPP tracking tests.

Table 1. Metrics for Best Performing Device from Figure 2A and the Device Metrics for Figure 2C

OCIL thickness (nm)	V_{OC} (V)	J_{SC} (mA/cm^2)	FF (%)	PCE (%)
best device	0.95	22.6	75.8	16.3
4	0.91 ± 0.06	20.49 ± 0.66	68.23 ± 3.81	12.72 ± 1.59
12	0.96 ± 0.01	20.96 ± 1.54	71.03 ± 3.23	14.35 ± 1.28
24	0.96 ± 0.01	21.22 ± 0.57	72.44 ± 2.47	14.82 ± 0.73
60	0.94 ± 0.01	22.64 ± 0.47	72.37 ± 1.65	15.37 ± 0.51
93	0.95 ± 0.02	20.21 ± 0.58	69.94 ± 1.46	13.44 ± 0.56
190	0.96 ± 0.01	18.33 ± 0.37	67.39 ± 2.79	11.92 ± 0.45

perovskite-based devices, which is particularly important when considering potential for scale-up and integration into commercial devices.

The influence of C_{60}/C_{70}-N on device stability was investigated further using maximum power point (MPP) tracking tests performed in an inert atmosphere glovebox (N_2 atmosphere, <1 ppm of O_2, <1 ppm of H_2O, Figure 2D). Under simulated AM1.5G irradiation (100 mW cm^{-2}), devices without an interlayer, and with ∼24, ∼60, and ∼93 nm interlayers, were held at their approximate MPP voltages (without interlayer, V_{max} = 0.6 V; with interlayer, V_{max} = 0.8 V), and the PCE of each device was measured every ∼400 s (Figure 2D). Devices without an interlayer showed poor stability, and their PCE declined rapidly by ∼60% within ∼500 s. Over the time frame of these measurements, devices containing interlayers exhibited much greater stability. For example, after ∼500 s the PCE values for devices with ∼24 nm and ∼60 nm OCILs started declining, while devices with thicker interlayers (∼93 nm) showed almost no degradation following the MPP tracking test, confirming the beneficial influence of OCIL thickness on device stability and the excellent tolerance of device performance to relatively thick interlayers.

To examine the mechanism underpinning device improvement and stabilization with C_{60}/C_{70}-N interlayers, we investigated the surface chemistry of interlayer-modified Ag electrodes by X-ray photoelectron spectroscopy (XPS) and ultraviolet photoelectron spectroscopy (UPS). As shown in Figure 3A, the Ag3d peaks shifted to lower binding energy after coating the metal with an ultrathin film of C_{60}/C_{70}-N (∼2 nm), indicating a strong interaction between the metal and fullerene

DOI: 10.1021/acscentsci.7b00454
ACS Cent. Sci. 2018, 4, 216–222

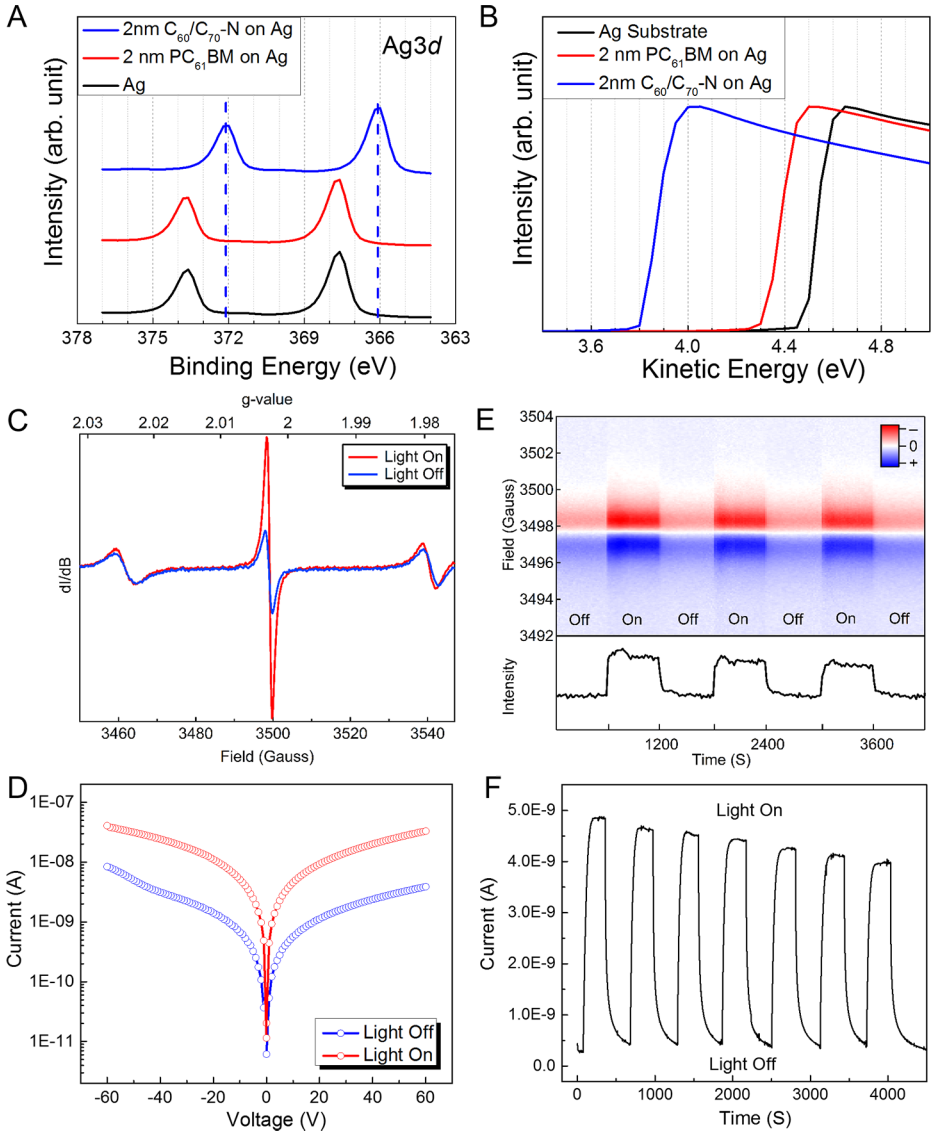

Figure 3. (A) XPS measurements of the Ag substrate with and without a C_{60}/C_{70}-N interlayer: high resolution Ag3d XPS spectra; (B) UPS measurements of Ag substrate with and without a C_{60}/C_{70}-N interlayer; (C) EPR spectra of C_{60}/C_{70}-N in toluene (~10 mg/mL, 200 μL); (D) I–V measurements of C_{60}/C_{70}-N thin film coated on parallel gold electrodes; (E) *in situ* photocharging EPR measurement; (F) photoswitching of a C_{60}/C_{70}-N thin film coated on parallel gold electrodes with a constant bias of 20 V.

mixture. This interaction was further confirmed by UPS, as a thin layer of C_{60}/C_{70}-N (~2 nm) provided a large negative interfacial dipole ($\Delta \sim -0.7$ eV), effectively decreasing the work function of Ag (Figure 3B). This in turn leads to an increase in the built-in electrostatic potential (V_{bi}) across the device, and increases device efficiency. In contrast, an ultrathin layer of $PC_{61}BM$ (~2 nm) yielded no significant interfacial dipole, inducing a low device PCE. The chemical passivation of the Ag electrode offered by these interlayers advantageously delays electrode corrosion from halide defects (e.g., I^-).[37]

Electron paramagnetic resonance (EPR) spectroscopy and conductivity measurements were performed to probe the electrical properties of C_{60}/C_{70}-N. The EPR spectra of C_{60}/C_{70}-N in the dark showed three transitions, with a central peak at 3498 G (g = 2.002) and a peak-to-peak line width of ΔH_{PP} = 1.4 G (Figure 3C). The central peak is assigned to the fullerene anions, due to the characteristic g value and its sharp line shape.[46] The two transitions spaced equidistant from the central peak are attributed to super hyperfine splitting generated by spin density spreading onto the ^{14}N atom with I = 1 nuclear spin. Moreover, the hyperfine splitting of A = 40 G with g = 2.002 confirmed the presence of radical cations on the tertiary amines.[47] Thus, the central peak arises from an overlap of the amine cation and C_{60}/C_{70} anion. As control experiments, EPR measurements of $PC_{61}BM$ and phenyl-C_{71}-butyric acid methyl ester ($PC_{71}BM$) produced no such signals (Figure S7A,C). Based on these results, and supported by density functional theory (DFT), the self-doping property of C_{60}/C_{70}-N mainly occurs by intramolecular electron transfer from the tertiary amines to the electron deficient fullerene. This is also seen in the individual EPR spectra of C_{60}-N and C_{70}-N (Figure S7A,C) and is consistent with a molecular dipole oriented from the fullerene cage to the tertiary amines.[48,49] Interestingly, the EPR signal intensified when irradiated with white light (70 mW cm^{-2}), indicative of photoenhanced self-doping (Figure 3C, Figure S7A,C). Current–voltage (I–V) measurements confirmed that photocurrent within the C_{60}/C_{70}-N thin films is nearly 1 order of magnitude larger than in

DOI: 10.1021/acscentsci.7b00454
ACS Cent. Sci. 2018, 4, 216–222

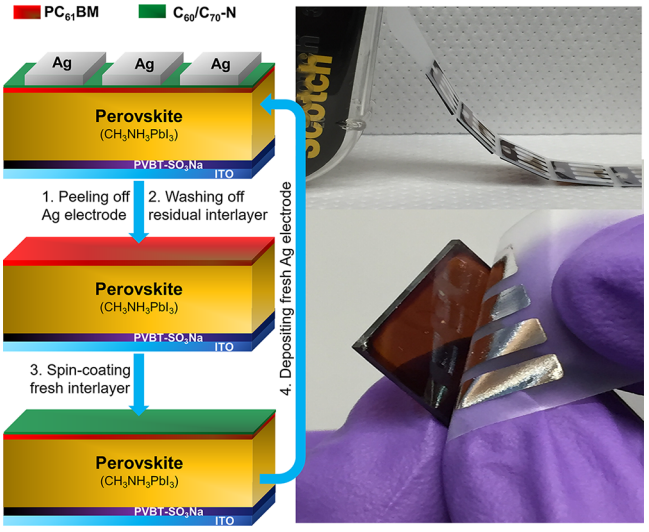

Figure 4. Repeel and replace process. Left: schematic of "peel and replace". Right: a photograph of the electrode peeling process performed simply by hand using Scotch tape.

the dark (Figure 3D). $PC_{61}BM$, on the other hand, showed negligible photocurrent gain, and $PC_{71}BM$ showed only slight photocurrent enhancement under the same conditions (Figure S7B,D). An *in situ* photocharging EPR measurement was performed to further investigate photoenhanced self-doping of C_{60}/C_{70}-N. As shown in Figure 3E, irradiation modulated the population of free radicals, which affords a reproducible on/off current cycling in C_{60}/C_{70}-N thin films (Figure 3F). This photoenhanced self-doping property affords a broad thickness processing window for C_{60}/C_{70}-N OCIL, while also enhancing chemical passivation in devices. Moreover, self-doping of C_{60}/C_{70}-N leads to higher conductivity without using external dopants, which improves stability of the perovskite active layer.

To exploit this chemical passivation in devices, the Ag electrode was removed by simply adhering Scotch tape (Figure 4) to the electrode and peeling it away. XPS analysis of the peeled metal (Ag) electrodes (Figure S8) revealed both Ag and N signals on the bottom surface, indicating partial removal of the interlayer during peeling. For example, after performing an MPP tracking test for ~4000 s, the Ag electrode was peeled away and XPS analysis of the bottom metal surface showed iodine on the electrodes from devices containing OCILs thinner than ~93 nm, while no iodine was found on the electrode for devices with >93 nm OCILs (Figure S8). This suggests that migration of I^- to the metal electrode, which has been identified as a perovskite degradation mechanism,[37] can be impeded by employing thicker OCILs. We speculate that thicker OCILs capture transient I^- impurities, due to the abundance of available tertiary amines. Furthermore, the generation of radical cations on the tertiary amines of C_{60}/C_{70}-N after electron transfer to fullerene aids iodide capture. Given that the formation of AgI at the CIL/Ag interface is known to contribute to device instability,[37] it would be ideal to completely remove corrosive halide ions. We sought to accomplish this using a peeling method, followed by replacement with a fresh OCIL and Ag electrode to essentially extract the ion contaminants passivated by the OCIL. Cross-sectional scanning electron microscopy (SEM) after removal of the Ag electrode revealed no observable damage to the layers within the device sample (Figure S9).

This peel and replace process was repeated three times to ensure the reliability of the technique, resulting in no apparent device degradation, as shown in Figure 5A (initial average PCE = 14.0 ± 0.7% for all 10 devices). The technique was performed following extended device irradiation (MPP tracking test for 4000 s) to accelerate ionic defect contamination from the perovskite photoactive layer to the OCIL and OCIL/Ag interface (Figure 5B). The device efficiency declined by >30%

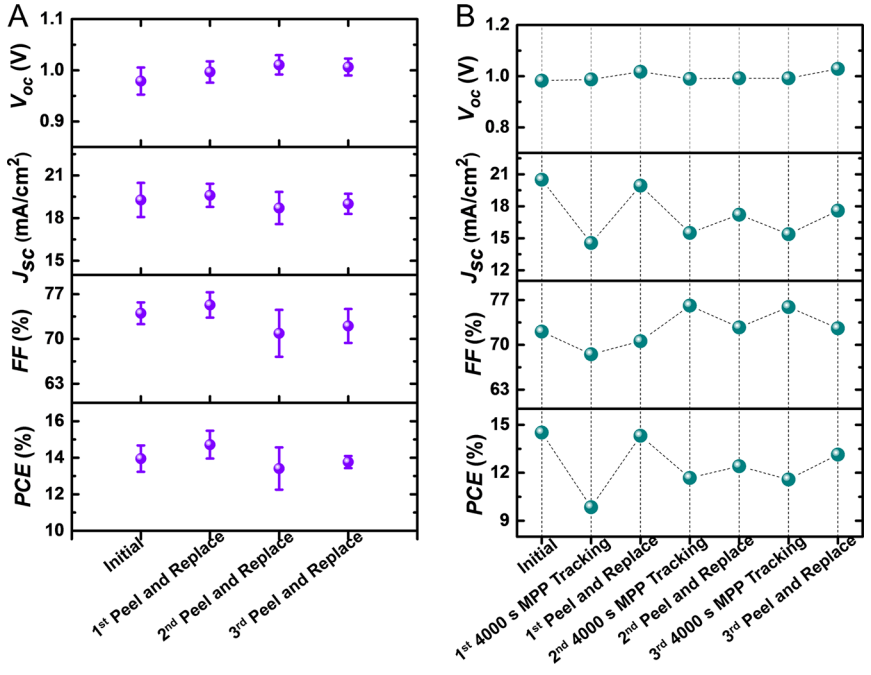

Figure 5. Applying repeel and replace to photovoltaic devices. (A) Three cycles of measurements based on 10 perovskite devices. (B) Sample device recovery measurement in three continuous cycles of MPP tracking tests (V_{max} = 0.8 V). J_{max} values from the MPP tracking tests are shown in Figure S11.

DOI: 10.1021/acscentsci.7b00454
ACS Cent. Sci. 2018, 4, 216−222

(from PCE = 14.5 to 9.8%) after an initial 4000 s MPP tracking test, but efficiency was recovered (PCE = 14.3%) essentially in full following the repeel and replace procedure (Figure 5B). Interestingly, irradiating the same device for an additional MPP tracking test of 4000 s led to less significant degradation (~20%, from PCE = 14.3 to 11.7%), which was revitalized in part by the peel and replace technique to give PCE = 12.4%. Repeating an additional 4000 s MPP tracking test, and peel and replace cycle, yielded a similar result as the second cycle, recovering the device PCE to 13.2%. Thus, three cycles of MPP degradation and electrode replacement resulted in only minor PCE decline, from 14.5% to 13.2%, which underscores the robustness of this process and the resulting perovskite solar cells, as shown in Figure 5B. XPS measurements performed on the top of the device, after reapplying a fresh OCIL by spin-coating, showed no iodine, further confirming that this method extracts detrimental ions near the metal electrode (Figure S10). This simple, consecutive repeel and replace procedure holds potential to further extend the lifetime of perovskite solar cells by recycling the perovskite active layer, providing a feasible method to detach and repeatedly replace the interlayer and electrodes.

CONCLUSION

A solution processable fulleropyrrolidine mixture (C_{60}/C_{70}-N) was developed and utilized as an efficient OCIL for perovskite solar cells with a maximum PCE of 16.3%. Exceptional insensitivity to the OCIL thickness, from ~4 to ~190 nm, was found with PCE values exceeding 12% across the entire thickness range due to photoenhanced self-doping of the interlayer. This fulleropyrrolidine mixture efficiently passivates the Ag electrode and traps halide ions (i.e., I^-) migrating from the perovskite active layer, resulting in enhanced device stability, as confirmed by XPS analysis and MPP tracking tests on devices with different OCIL thicknesses. Furthermore, degraded devices were revitalized by peeling and replacing the OCIL/Ag electrode, resulting in improved device stability upon repeated cycles with little change to the overall device PCE. This electrode and device regeneration technique represents a general method that is anticipated to apply broadly to numerous OCIL materials and open new pathways to overcome the intrinsic instability of perovskite-based devices.

ASSOCIATED CONTENT

Supporting Information

The Supporting Information is available free of charge on the ACS Publications website at DOI: 10.1021/acscentsci.7b00454.

Experimental details, material synthesis, device characterizations, XPS data, and SEM data (PDF)

AUTHOR INFORMATION

Corresponding Authors

*E-mail: russell@mail.pse.umass.edu.
*E-mail: tsemrick@mail.pse.umass.edu.

ORCID

Zachariah A. Page: 0000-0002-1013-5422
Volodimyr V. Duzhko: 0000-0001-9951-2599
Kevin R. Kittilstved: 0000-0002-9852-7454
Todd Emrick: 0000-0003-0460-1797
Thomas P. Russell: 0000-0001-6384-5826

Present Address

§Z.A.P.: Materials Research Laboratory, University of California at Santa Barbara, Santa Barbara, CA 93106-5121, United States.

Notes

The authors declare no competing financial interest.

ACKNOWLEDGMENTS

Y.L. and T.P.R. were supported by the Office of Naval Research, Materials Division, under Contract N00014-15-1-2244. The authors acknowledge the support of NSF-CHE 1506839 (T.E.) and the W.M. Keck Electron Microscopy for SEM and Nanostructures Laboratory for AFM measurements. Photovoltaic device fabrication and characterization and UPS measurements were performed in the Laboratory for Electronic Materials and Devices at UMASS.

REFERENCES

(1) Gratzel, M. The light and shade of perovskite solar cells. *Nat. Mater.* **2014**, *13*, 838−842.
(2) Green, M. A.; Ho-Baillie, A.; Snaith, H. J. The emergence of perovskite solar cells. *Nat. Photonics* **2014**, *8*, 506−514.
(3) Meng, L.; You, J.; Guo, T.-F.; Yang, Y. Recent Advances in the Inverted Planar Structure of Perovskite Solar Cells. *Acc. Chem. Res.* **2016**, *49*, 155−165.
(4) Zhao, Y.; Zhu, K. Organic-inorganic hybrid lead halide perovskites for optoelectronic and electronic applications. *Chem. Soc. Rev.* **2016**, *45*, 655−689.
(5) Yang, S.; Fu, W.; Zhang, Z.; Chen, H.; Li, C.-Z. Recent advances in perovskite solar cells: efficiency, stability and lead-free perovskite. *J. Mater. Chem. A* **2017**, *5*, 11462−11482.
(6) Burschka, J.; Pellet, N.; Moon, S.-J.; Humphry-Baker, R.; Gao, P.; Nazeeruddin, M. K.; Gratzel, M. Sequential deposition as a route to high-performance perovskite-sensitized solar cells. *Nature* **2013**, *499*, 316−319.
(7) Liu, M.; Johnston, M. B.; Snaith, H. J. Efficient planar heterojunction perovskite solar cells by vapour deposition. *Nature* **2013**, *501*, 395−398.
(8) Zhou, H.; Chen, Q.; Li, G.; Luo, S.; Song, T.-b.; Duan, H.-S.; Hong, Z.; You, J.; Liu, Y.; Yang, Y. Interface engineering of highly efficient perovskite solar cells. *Science* **2014**, *345*, 542−546.
(9) Jeon, N. J.; Noh, J. H.; Yang, W. S.; Kim, Y. C.; Ryu, S.; Seo, J.; Seok, S. I. Compositional engineering of perovskite materials for high-performance solar cells. *Nature* **2015**, *517*, 476−480.
(10) Mei, A.; Li, X.; Liu, L.; Ku, Z.; Liu, T.; Rong, Y.; Xu, M.; Hu, M.; Chen, J.; Yang, Y.; Grätzel, M.; Han, H. A hole-conductor−free, fully printable mesoscopic perovskite solar cell with high stability. *Science* **2014**, *345*, 295−298.
(11) Nie, W.; Tsai, H.; Asadpour, R.; Blancon, J.-C.; Neukirch, A. J.; Gupta, G.; Crochet, J. J.; Chhowalla, M.; Tretiak, S.; Alam, M. A.; Wang, H.-L.; Mohite, A. D. High-efficiency solution-processed perovskite solar cells with millimeter-scale grains. *Science* **2015**, *347*, 522−525.
(12) Xiao, Z.; Dong, Q.; Bi, C.; Shao, Y.; Yuan, Y.; Huang, J. Solvent Annealing of Perovskite-Induced Crystal Growth for Photovoltaic-Device Efficiency Enhancement. *Adv. Mater.* **2014**, *26*, 6503−6509.
(13) Liang, P.-W.; Liao, C.-Y.; Chueh, C.-C.; Zuo, F.; Williams, S. T.; Xin, X.-K.; Lin, J.; Jen, A. K. Y. Additive Enhanced Crystallization of Solution-Processed Perovskite for Highly Efficient Planar-Heterojunction Solar Cells. *Adv. Mater.* **2014**, *26*, 3748−3754.
(14) Heo, J. H.; Han, H. J.; Kim, D.; Ahn, T. K.; Im, S. H. Hysteresis-less inverted CH3NH3PbI3 planar perovskite hybrid solar cells with 18.1% power conversion efficiency. *Energy Environ. Sci.* **2015**, *8*, 1602−1608.
(15) Xie, F.; Chen, C.-C.; Wu, Y.; Li, X.; Cai, M.; Liu, X.; Yang, X.; Han, L. Vertical recrystallization for highly efficient and stable formamidinium-based inverted-structure perovskite solar cells. *Energy Environ. Sci.* **2017**, *10*, 1942−1949.

DOI: 10.1021/acscentsci.7b00454
ACS Cent. Sci. 2018, 4, 216−222

(16) https://commons.wikimedia.org/wiki/File:Best_Research-Cell_Efficiencies.png.
(17) Correa-Baena, J.-P.; Abate, A.; Saliba, M.; Tress, W.; Jesper Jacobsson, T.; Gratzel, M.; Hagfeldt, A. The rapid evolution of highly efficient perovskite solar cells. *Energy Environ. Sci.* **2017**, *10*, 710−727.
(18) Wang, D.; Wright, M.; Elumalai, N. K.; Uddin, A. Stability of perovskite solar cells. *Sol. Energy Mater. Sol. Cells* **2016**, *147*, 255−275.
(19) Tiep, N. H.; Ku, Z.; Fan, H. J. Recent Advances in Improving the Stability of Perovskite Solar Cells. *Adv. Energy. Mater.* **2016**, *6*, 1501420.
(20) Lee, M. M.; Teuscher, J.; Miyasaka, T.; Murakami, T. N.; Snaith, H. J. Efficient Hybrid Solar Cells Based on Meso-Superstructured Organometal Halide Perovskites. *Science* **2012**, *338*, 643−647.
(21) Berhe, T. A.; Su, W.-N.; Chen, C.-H.; Pan, C.-J.; Cheng, J.-H.; Chen, H.-M.; Tsai, M.-C.; Chen, L.-Y.; Dubale, A. A.; Hwang, B.-J. Organometal halide perovskite solar cells: degradation and stability. *Energy Environ. Sci.* **2016**, *9*, 323−356.
(22) Kato, Y.; Ono, L. K.; Lee, M. V.; Wang, S.; Raga, S. R.; Qi, Y. Perovskite Solar Cells: Silver Iodide Formation in Methyl Ammonium Lead Iodide Perovskite Solar Cells with Silver Top Electrodes (Adv. Mater. Interfaces 13/2015). *Adv. Mater. Interfaces* **2015**, *2*, 1500195.
(23) Guarnera, S.; Abate, A.; Zhang, W.; Foster, J. M.; Richardson, G.; Petrozza, A.; Snaith, H. J. Improving the Long-Term Stability of Perovskite Solar Cells with a Porous Al2O3 Buffer Layer. *J. Phys. Chem. Lett.* **2015**, *6*, 432−437.
(24) Domanski, K.; Correa-Baena, J.-P.; Mine, N.; Nazeeruddin, M. K.; Abate, A.; Saliba, M.; Tress, W.; Hagfeldt, A.; Grätzel, M. Not All That Glitters Is Gold: Metal-Migration-Induced Degradation in Perovskite Solar Cells. *ACS Nano* **2016**, *10*, 6306−6314.
(25) Leijtens, T.; Eperon, G. E.; Pathak, S.; Abate, A.; Lee, M. M.; Snaith, H. J. Overcoming ultraviolet light instability of sensitized TiO2 with meso-superstructured organometal tri-halide perovskite solar cells. *Nat. Commun.* **2013**, *4*, 2885.
(26) Liu, Y.; Bag, M.; Renna, L. A.; Page, Z. A.; Kim, P.; Emrick, T.; Venkataraman, D.; Russell, T. P. Understanding Interface Engineering for High-Performance Fullerene/Perovskite Planar Heterojunction Solar Cells. *Adv. Energy. Mater.* **2016**, *6*, 1501606.
(27) Li, Y.; Lu, K.; Ling, X.; Yuan, J.; Shi, G.; Ding, G.; Sun, J.; Shi, S.; Gong, X.; Ma, W. High performance planar-heterojunction perovskite solar cells using amino-based fulleropyrrolidine as the electron transporting material. *J. Mater. Chem. A* **2016**, *4*, 10130−10134.
(28) Li, Y.; Zhao, Y.; Chen, Q.; Yang, Y.; Liu, Y.; Hong, Z.; Liu, Z.; Hsieh, Y.-T.; Meng, L.; Li, Y.; Yang, Y. Multifunctional Fullerene Derivative for Interface Engineering in Perovskite Solar Cells. *J. Am. Chem. Soc.* **2015**, *137*, 15540−15547.
(29) You, J.; Meng, L.; Song, T.-B.; Guo, T.-F.; Yang, Y.; Chang, W.-H.; Hong, Z.; Chen, H.; Zhou, H.; Chen, Q.; Liu, Y.; De Marco, N.; Yang, Y. Improved air stability of perovskite solar cells via solution-processed metal oxide transport layers. *Nat. Nanotechnol.* **2016**, *11*, 75−81.
(30) Reddy, S. S.; Gunasekar, K.; Heo, J. H.; Im, S. H.; Kim, C. S.; Kim, D.-H.; Moon, J. H.; Lee, J. Y.; Song, M.; Jin, S.-H. Highly Efficient Organic Hole Transporting Materials for Perovskite and Organic Solar Cells with Long-Term Stability. *Adv. Mater.* **2016**, *28*, 686−693.
(31) Kim, G.-W.; Kang, G.; Kim, J.; Lee, G.-Y.; Kim, H. I.; Pyeon, L.; Lee, J.; Park, T. Dopant-free polymeric hole transport materials for highly efficient and stable perovskite solar cells. *Energy Environ. Sci.* **2016**, *9*, 2326−2333.
(32) Liu, Y.; Hong, Z.; Chen, Q.; Chen, H.; Chang, W.-H.; Yang, Y.; Song, T.-B.; Yang, Y. Perovskite Solar Cells Employing Dopant-Free Organic Hole Transport Materials with Tunable Energy Levels. *Adv. Mater.* **2016**, *28*, 440−446.
(33) Nishimura, H.; Ishida, N.; Shimazaki, A.; Wakamiya, A.; Saeki, A.; Scott, L. T.; Murata, Y. Hole-Transporting Materials with a Two-Dimensionally Expanded π-System around an Azulene Core for Efficient Perovskite Solar Cells. *J. Am. Chem. Soc.* **2015**, *137*, 15656−15659.
(34) Rakstys, K.; Abate, A.; Dar, M. I.; Gao, P.; Jankauskas, V.; Jacopin, G.; Kamarauskas, E.; Kazim, S.; Ahmad, S.; Grätzel, M.; Nazeeruddin, M. K. Triazatruxene-Based Hole Transporting Materials for Highly Efficient Perovskite Solar Cells. *J. Am. Chem. Soc.* **2015**, *137*, 16172−16178.
(35) Huang, C.; Fu, W.; Li, C.-Z.; Zhang, Z.; Qiu, W.; Shi, M.; Heremans, P.; Jen, A. K. Y.; Chen, H. Dopant-Free Hole-Transporting Material with a C3h Symmetrical Truxene Core for Highly Efficient Perovskite Solar Cells. *J. Am. Chem. Soc.* **2016**, *138*, 2528−2531.
(36) Kranthiraja, K.; Gunasekar, K.; Kim, H.; Cho, A.-N.; Park, N.-G.; Kim, S.; Kim, B. J.; Nishikubo, R.; Saeki, A.; Song, M.; Jin, S.-H. High-Performance Long-Term-Stable Dopant-Free Perovskite Solar Cells and Additive-Free Organic Solar Cells by Employing Newly Designed Multirole π-Conjugated Polymers. *Adv. Mater.* **2017**, *29*, 1700183.
(37) Back, H.; Kim, G.; Kim, J.; Kong, J.; Kim, T. K.; Kang, H.; Kim, H.; Lee, J.; Lee, S.; Lee, K. Achieving long-term stable perovskite solar cells via ion neutralization. *Energy Environ. Sci.* **2016**, *9*, 1258−1263.
(38) Domanski, K.; Roose, B.; Matsui, T.; Saliba, M.; Turren-Cruz, S.-H.; Correa-Baena, J.-P.; Carmona, C. R.; Richardson, G.; Foster, J. M.; De Angelis, F.; Ball, J. M.; Petrozza, A.; Mine, N.; Nazeeruddin, M. K.; Tress, W.; Gratzel, M.; Steiner, U.; Hagfeldt, A.; Abate, A. Migration of cations induces reversible performance losses over day/night cycling in perovskite solar cells. *Energy Environ. Sci.* **2017**, *10*, 604−613.
(39) Guerrero, A.; You, J.; Aranda, C.; Kang, Y. S.; Garcia-Belmonte, G.; Zhou, H.; Bisquert, J.; Yang, Y. Interfacial Degradation of Planar Lead Halide Perovskite Solar Cells. *ACS Nano* **2016**, *10*, 218−224.
(40) Page, Z. A.; Liu, Y.; Duzhko, V. V.; Russell, T. P.; Emrick, T. Fulleropyrrolidine interlayers: Tailoring electrodes to raise organic solar cell efficiency. *Science* **2014**, *346*, 441−444.
(41) http://www.mtr-ltd.com/PriceList.htm.
(42) Urbani, M.; Pelado, B.; de la Cruz, P.; Yamanaka, K.-i.; Ito, O.; Langa, F. Synthesis and Photoinduced Energy- and Electron-Transfer Processes of C60−Oligothienylenevinylene−C70 Dumbbell Compounds. *Chem. - Eur. J.* **2011**, *17*, 5432−5444.
(43) Boudon, C.; Gisselbrecht, J.-P.; Gross, M.; Herrmann, A.; Rüttimann, M.; Crassous, J.; Cardullo, F.; Echegoyen, L.; Diederich, F. Redox Characteristics of Covalent Derivatives of the Higher Fullerenes C70, C76, and C78. *J. Am. Chem. Soc.* **1998**, *120*, 7860−7868.
(44) Liu, Y.; Renna, L. A.; Page, Z. A.; Thompson, H. B.; Kim, P. Y.; Barnes, M. D.; Emrick, T.; Venkataraman, D.; Russell, T. P. A Polymer Hole Extraction Layer for Inverted Perovskite Solar Cells from Aqueous Solutions. *Adv. Energy. Mater.* **2016**, *6*, 1600664.
(45) Page, Z. A.; Liu, Y.; Puodziukynaite, E.; Russell, T. P.; Emrick, T. Hydrophilic Conjugated Polymers Prepared by Aqueous Horner−Wadsworth−Emmons Coupling. *Macromolecules* **2016**, *49*, 2526−2532.
(46) Reed, C. A.; Bolskar, R. D. Discrete fulleride anions and fullerenium cations. *Chem. Rev.* **2000**, *100*, 1075−1119.
(47) Symons, M. C. R. Formation of the Dimethylamino Radical from the Radical Cation of Tetramethylurea - an Electron-Spin Resonance-Radiation Chemical Study. *J. Chem. Soc., Chem. Commun.* **1986**, 11−12.
(48) Lee, H.; Stephenson, J. C.; Richter, L. J.; McNeill, C. R.; Gann, E.; Thomsen, L.; Park, S.; Jeong, J.; Yi, Y.; DeLongchamp, D. M.; Page, Z. A.; Puodziukynaite, E.; Emrick, T.; Briseno, A. L. The Structural Origin of Electron Injection Enhancements with Fulleropyrrolidine Interlayers. *Adv. Mater. Interfaces* **2016**, *3*, 1500852.
(49) Karak, S.; Page, Z. A.; Tinkham, J. S.; Lahti, P. M.; Emrick, T.; Duzhko, V. V. Raising efficiency of organic solar cells with electrotropic additives. *Appl. Phys. Lett.* **2015**, *106*, 103303.

DOI: 10.1021/acscentsci.7b00454
ACS Cent. Sci. 2018, 4, 216−222